

VIP Very Important Paper

www.batteries-supercaps.org

# Crack Suppression by Downsizing Sulfide-Electrolyte Particles for High-Current-Density Operation of Metal/Alloy Anodes

Han-Seul Kim,<sup>[a]</sup> Kenta Watanabe,<sup>[a]</sup> Naoki Matsui,<sup>[b]</sup> Kota Suzuki,<sup>[b]</sup> Ryoji Kanno,<sup>[b]</sup> and Masaaki Hirayama<sup>\*[a, b]</sup>

Stable physical contact between lithium metal/alloy anodes and the solid electrolyte layer is crucial for the durable operation of all-solid-state batteries. Herein, we have attempted to control the mechanical properties of a Li<sub>10.35</sub>Ge<sub>1.35</sub>P<sub>1.65</sub>S<sub>12</sub> (LGPS) solid electrolyte layer by the grain size and examined the mechanical strength against stresses originating from volumetric changes of an In-Li anode layer. The submicron-sized LGPS electrolyte ( $d_{50}$ : 0.51 μm) with a uniform particle size distribution was successfully fabricated by a wet-milling process. The crystallinity of LGPS negligibly changes on pulverization. In-Li symmetric

cells with the wet-milled LGPS exhibit higher cycle stability than those constructed with micro-sized LGPS ( $d_{50}$ : 1.32 μm), not well-controlled by particle size, owing to greater suppression of overvoltage generation and growth. Microstructural analyses have revealed that the small and uniform LGPS particles are less prone to physical degradation (cracking) owing to volume changes of In-Li. Downsizing of solid electrolytes is a good strategy for developing physically stable electrode/solid electrolyte interfaces even at high current density operation.

## Introduction

All-solid-state batteries (ASSBs) comprising thermally stable inorganic electrodes and solid electrolytes have gained prominence as next-generation batteries with high energy density and reliability.<sup>[1–4]</sup> Electrons and ions involved in electrochemical reactions are transported through physical contact between the constituent materials of ASSBs; therefore, the electrode-electrolyte contact area determines the power density and cycle stability.<sup>[5,6]</sup> Sulfide electrolytes exhibit significantly higher deformability than oxide electrolytes,<sup>[7,8]</sup> enabling sufficient contact-area formation between the electrolytes and at the electrode/electrolyte interface. Furthermore, their excellent ionic conductivity facilitates the construction of high-performance ASSBs. However, to improve the cycle characteristics and increase the practicability of sulfide electrolyte-based ASSBs, it is vital to ensure sufficient physical contact.<sup>[9–13]</sup> In particular,

lithium metal and alloy anodes with high theoretical capacities of  $> 1000 \text{ mAh g}^{-1}$  undergo large volume changes of  $> 100\%$  owing to lithiation/delithiation during charging and discharging.<sup>[14,15]</sup> This causes cracks between the electrode and electrolyte during charging and discharging.<sup>[16–20]</sup> Unlike liquid electrolytes, solid electrolytes cannot penetrate the inter-particle spaces, leading to an irreversible loss of particle-to-particle contact at the interfaces.<sup>[5,13]</sup> It remains challenging to maintain a sufficient electrode-electrolyte contact area with metal and alloy anodes by suppressing crack formation.

The downsizing of solid-electrolyte particles has been used to improve the electrode-electrolyte mixing state and increase the capacity of the ASSBs.<sup>[21–23]</sup> An increase in the initial contact area is assumed to maintain sufficient conduction pathways for battery reactions, even after a physical-contact reduction (owing to volume changes during cycling). According to grain boundary strengthening (or Hall-Petch strengthening), materials with a small grain size exhibit high mechanical strength (tensile strength, hardness, and plasticity).<sup>[24,25]</sup> The yield strength of small-particle materials is enhanced as greater stress is required for dislocation movement in such systems. A small grain size increases the grain boundaries, enhancing the resistance to dislocation pile-up. Moreover, the formation of less dislocation pile-up increases the stress to deform grains.<sup>[26]</sup> For example, MgO pellets comprising large grains ( $> 50 \mu\text{m}$ ) exhibit significantly lower yielding strength than those comprising sub-micrometer-sized grains owing to a lower grain boundary density.<sup>[27]</sup> This material-development strategy involving grain size reduction has been widely utilized in polymers, ceramics, and powder metallurgy.<sup>[28–31]</sup> However, reports on the effect of the size distribution of solid electrolytes on their mechanical properties and ASSB performance are scarce.

[a] H.-S. Kim, Prof. K. Watanabe, Prof. M. Hirayama  
Department of Chemical Science and Engineering,  
School of Materials and Chemical Technology,  
Tokyo Institute of Technology,  
4259 Nagatsuta, Midori-ku, Yokohama 226-8502, Japan  
E-mail: hirayama@mac.titech.ac.jp

[b] Prof. N. Matsui, Prof. K. Suzuki, Prof. R. Kanno, Prof. M. Hirayama  
Research Center for All-Solid-State Battery,  
Institute of Innovative Research,  
Tokyo Institute of Technology,  
4259 Nagatsuta, Midori-ku, Yokohama 226-8502, Japan

Supporting information for this article is available on the WWW under <https://doi.org/10.1002/batt.202300306>

© 2023 The Authors. *Batteries & Supercaps* published by Wiley-VCH GmbH. This is an open access article under the terms of the Creative Commons Attribution License, which permits use, distribution and reproduction in any medium, provided the original work is properly cited.

To control the size distribution of crystalline solid electrolytes, small particles can be fabricated using liquid-phase synthesis (bottom-up), pulverization, and classification (top-down).<sup>[32]</sup> Over the past few years, liquid-phase chemistry has significantly increased the scalability of sulfide electrolytes.<sup>[33,34]</sup> However, the products of liquid-phase synthesis are dried at low temperatures to suppress decomposition; therefore, they often exhibit low crystallinity and contain residual-solvent impurities. The pulverization process (with a high kinetic-energy milling process) also generates low-crystallinity products. Therefore, these processes are mainly used to synthesize glass electrolytes.<sup>[21,35]</sup> Sieve classification isolates particles smaller than the hole size of the sieve, without disrupting their chemical composition and crystallinity. However, limitations in the sieve-hole size permit only a few micrometers of sieve refinement. Therefore, to clarify the particle-size effect on the mechanical properties of electrolytes (in isolation from ionic-conductivity changes), it is vital to develop an efficient method to downsize electrolyte particles.

This study reports the fabrication of sub-micrometer-sized  $\text{Li}_{10}\text{GeP}_2\text{S}_{12}$  (LGPS) solid electrolytes with a small size distribution by wet milling with relatively mild pulverization conditions compared to conventional dry milling, along with their electrochemical and mechanical properties. The morphology, crystallinity, and lithium super ionic conductivity of the wet-milled (WM) and hand-milled (HM) LGPS were investigated using scanning electron microscopy (SEM), X-ray diffraction (XRD), and electrochemical impedance spectroscopy (EIS). The electrochemical properties and microstructural changes in In-Li/size-controlled LGPS/In-Li symmetric cells were investigated to clarify the mechanical strength at the In-Li/LGPS interface, which is known to be chemically stable.<sup>[36,37]</sup> The current-density range for the mechanically stable operation of all-solid-state cells with In-Li counter electrodes was also investigated.

## Results and Discussion

### Structures and ionic conductivities of LGPS with different particle sizes

Figure 1(a) shows the XRD patterns of HM-LGPS (pulverized for 5 and 30 min, labeled HM(5 min)-LGPS and HM(30 min)-LGPS, respectively) and WM-LGPS. All the spectra contain diffraction peaks corresponding to  $\text{Li}_{10.35}\text{Ge}_{1.35}\text{P}_{1.65}\text{S}_{12}$  (a type of LGPS with the space group  $P4_2/nmc$ )<sup>[1]</sup> and some diffraction peaks at 15.8°, 18.0°, and 26.2° corresponding to  $\beta\text{-Li}_3\text{PS}_4$ <sup>[38]</sup> (as the secondary phase). The diffraction peaks of each sample exhibit similar widths, confirming that the milling conditions do not affect the crystallinity of the LGPS particles. The SEM images and dispersed particle-size distributions of LGPS are shown in Figure 1(b and c). The HM(5 min)-LGPS comprises small particles (a few micrometers in size) and coarse particles (larger than 20  $\mu\text{m}$ ). This is consistent with the crystal growth of LGPS during high-temperature sintering; the ground precursor mixtures contain particles that are a few micrometers in size. The frequency of coarse particles significantly decreases for HM(30 min)-LGPS, indicating that prolonged hand milling transforms coarse particles into smaller particles. Notably, HM(30 min)-LGPS shows a similar particle size distribution below 10  $\mu\text{m}$  as that of HM(5 min)-LGPS. This indicates that the LGPS particles could not be ground to a sub-micrometer or smaller size by hand milling. The SEM image of WM-LGPS indicates no coarse particles, with smaller particles than those observed in the SEM images of HM-LGPS. WM-LGPS exhibited a narrow size distribution with an average particle size ( $d_{50}$ ) of 0.51  $\mu\text{m}$ , which was significantly smaller than the  $d_{50}$  values of HM(5 min)- and HM(30 min)-LGPS (1.73  $\mu\text{m}$  and 1.32  $\mu\text{m}$ , respectively). We also investigated the morphologies of LGPS fabricated under different WM conditions. Although LGPS samples WM under faster rotation speeds and for longer durations showed a more

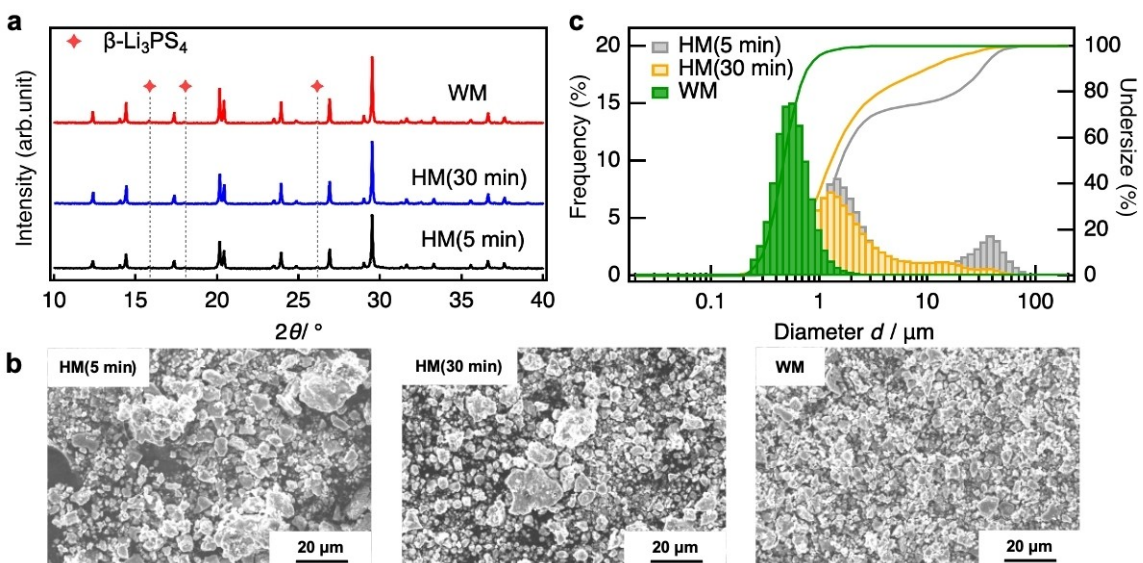


**Figure 1.** a) XRD patterns, b) SEM images (magnification factor:  $\times 1000$ ), and c) dispersed particle-size distributions of  $\text{Li}_{10.35}\text{Ge}_{1.35}\text{P}_{1.65}\text{S}_{12}$  pulverized under different milling conditions (HM(5 min): hand-milled for 5 min; HM(30 min): hand-milled for 30 min; and WM: wet-milled for 80 min).

uniform size distribution with smaller particles, they exhibited a significantly low crystallinity (details are provided in Supporting information S1). Therefore, the following wet-milling conditions were subsequently used for experimentation: ball-sizes of  $\varphi 5$  and  $\varphi 10$  mm; rotating speed of 300 rpm; and duration of 80 min. Figure 2 shows the Nyquist plots of the EIS results of HM(5 min)-, HM(30 min)-, and WM-LGPS at 298 and 175 K. At 298 K, a low-frequency semicircle edge and straight line, which corresponded to the ionic-conduction and interfacial resistance between the LGPS and Au electrodes, respectively, are observed for all samples. HM(5 min)-, HM(30 min)-, and WM-LGPS exhibited total ionic conductivities of 11.7, 10.1, and  $3.1 \text{ mS cm}^{-1}$  (calculated using the resistance estimated from the intersection of the straight line and the real axis,  $Z'$ ). To investigate the low conductivity of WM-LGPS, the bulk and grain boundary resistances for Li diffusion ( $R_b$  and  $R_{gb}$ , respectively) should be separated. Clear semicircles were not observed at 298 K in the measured frequency regions because of the small ionic-diffusion resistance of LGPS, which can be expressed by the following equation:

$$RC = 1/2\pi f_{top} \quad (1)$$

where  $R$  and  $C$  indicate the resistance and capacitance of the resistive components, respectively, and  $f_{top}$  is the frequency corresponding to the semicircular apex. At low temperatures, the semicircle of the resistive component should shift to lower

frequencies, as the resistance increases significantly. The Nyquist plots collected at 175 K show a small semicircle at a high frequency and a relatively large semicircle at a low frequency, which can be attributed to the bulk and grain boundary resistances, respectively.<sup>[39]</sup> Thus, the Nyquist plots were fitted using an equivalent circuit ( $R_b CPE_b R_{gb} CPE_{gb}$ ) comprising a parallel circuit of  $R$  and a constant-phase element (CPE). Table 1 summarizes the  $R_b$  and  $R_{gb}$  values at 175 K for each LGPS. HM(5 min)-, HM(30 min)-, and WM-LGPS exhibit  $R_b$  values of  $1.1 \times 10^4$ ,  $1.5 \times 10^4$ , and  $1.2 \times 10^4 \Omega$ , respectively. Enlarged images of the  $R_b$  semicircles at high frequencies are shown in Figure S3. These results confirm the absence of significant changes in crystal structure and crystallinity, consistent with the results of XRD analysis. Notably, WM-LGPS exhibited an  $R_{gb}$  value of  $10.2 \times 10^4 \Omega$ , which is 3.1 times larger than that of HM(5 min)-LGPS ( $3.3 \times 10^4 \Omega$ ). The number of grain boundaries in the samples increased depending on the surface area of the particles. Assuming the LGPS particles to be spherical, their surface-area increment is proportional to the square of the radius. The  $r^2$  value of the WM-LGPS particles, estimated using the average particle size as the diameter, is approximately 10 times larger than that of the HM(5 min)-LGPS particles. Thus, it could be speculated that the large  $R_{gb}$  of WM-LGPS could be mainly attributable to the large number of grain boundaries, and the WM process causes negligible degradation at the LGPS surfaces. Therefore, WM can be used as an effective technique for downsizing LGPS-type sulfide electrolytes without disrupting their high crystallinity.

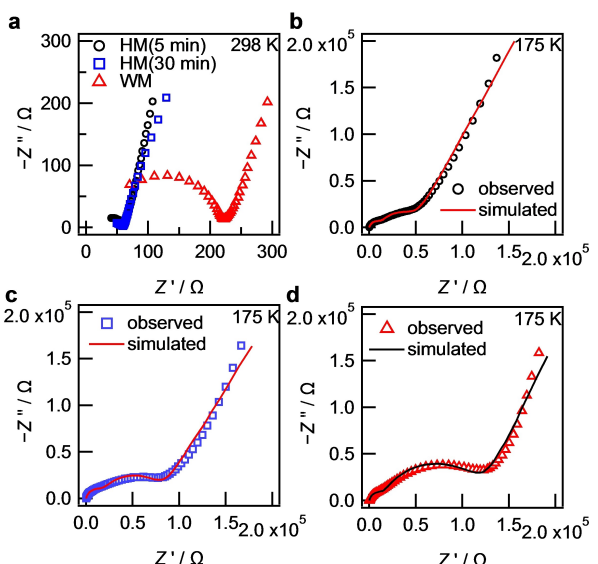


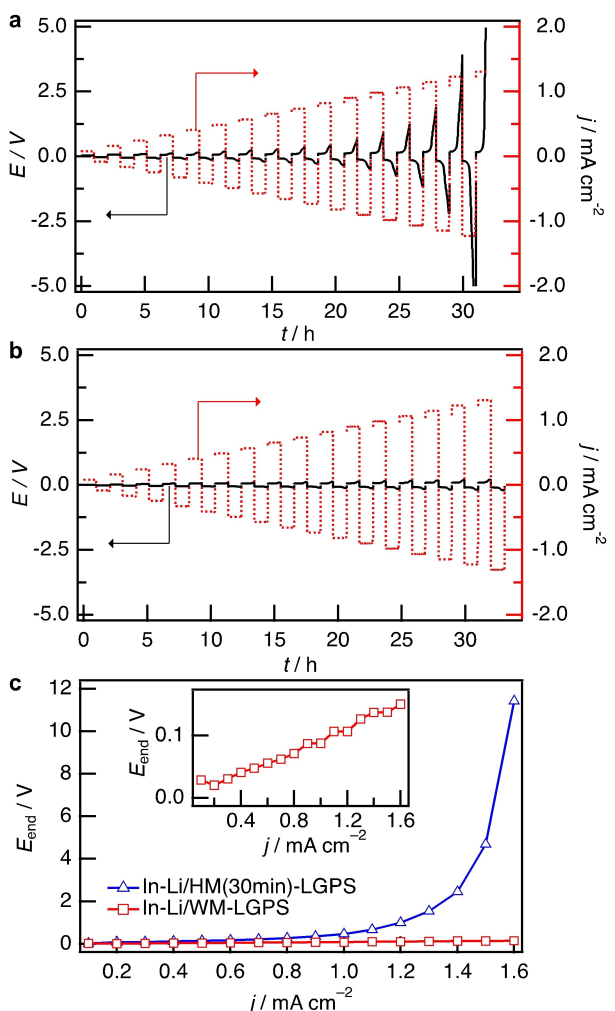
Figure 2. Nyquist plots of the HM(5 min)-, HM(30 min)-, and WM-LGPS EIS data at a) 298 and b-d) 175 K.

Table 1. Refined bulk and grain boundary resistances ( $R_b$  and  $R_{gb}$ , respectively) of different LGPS samples at 175 K.

Samples	$R_b [\Omega]$	$R_{gb} [\Omega]$
HM(5 min)-LGPS	$1.1 \times 10^4$	$3.3 \times 10^4$
HM(30 min)-LGPS	$1.5 \times 10^4$	$6.0 \times 10^4$
WM-LGPS	$1.2 \times 10^4$	$10.2 \times 10^4$

### Electrochemical properties of the In-Li/LGPS interface

Charge-discharge measurements for In-Li/LGPS/In-Li symmetric cells with HM(30 min)-LGPS and WM-LGPS were used to investigate the particle-size effect of solid electrolytes on the electrochemical stability of metal anodes. Indium-lithium alloys are likely to form a more chemically stable interface with sulfide electrolytes than lithium metal,<sup>[40-42]</sup> making it easier to investigate the physical effects. Figure 3 shows the cell-voltage variation at different current densities. The cells were charged and discharged for 1 h at different current densities (in the range of  $0.1$ – $1.6 \text{ mA cm}^{-2}$ ) at a rate of  $0.1 \text{ mA cm}^{-2}$  per cycle. In both the In-Li alloy electrodes, lithium alloying, and dealloying reactions occur at  $0.6 \text{ V}$  vs. In-Li.<sup>[37]</sup> For the cell with HM(30 min)-LGPS, negligible changes in voltage were observed during charge-discharge at  $0.1$  and  $0.2 \text{ mA cm}^{-2}$ , indicating stable lithium alloying and dealloying reactions at the In-Li/HM-LGPS interface. However, above  $0.3 \text{ mA cm}^{-2}$ , the cell voltage gradually increased during the reactions, particularly at the end of charge-discharge. This could correspond to the increase in the overpotential of lithium alloying and dealloying reactions. The overvoltage further increased with the current density and/or cycle number; it increased significantly (to over 5 V) during charging at  $1.6 \text{ mA cm}^{-2}$  and charge-discharge at current densities in the range of  $0.8$ – $1.6 \text{ cm}^{-2}$ . In contrast, the cell with WM-LGPS did not exhibit significant changes in voltage during charge-discharge below  $0.7 \text{ mA cm}^{-2}$ , despite the relatively low



**Figure 3.** Cell voltages of a) In-Li/HM(30 min)-LGPS/In-Li and b) In-Li/WM-LGPS/In-Li symmetric cells during charge and discharge (for 1 h) at different current densities in the range of  $0.1\text{--}1.6 \text{ mA cm}^{-2}$ . c) Cell-voltage variation at the end of the charging process. The inset in c depicts the magnified view of  $E_{\text{end}}$  vs.  $j$  for In-Li/WM-LGPS.

total ionic conductivity of the WM-LGPS layer. The increase in overvoltage was significantly suppressed to  $<0.15 \text{ V}$  at higher current densities. Furthermore, the overvoltage collected at the end of charging (applying a positive current) showed a linear relationship with the current density. Thus, the internal resistance of the In-Li/LGPS/In-Li cell negligibly changed during the cycling. The facilitated Li alloying and dealloying in the WM-LGPS electrolyte with the relatively low total ionic conductivity indicated that the rate-limiting step for lithium alloying and dealloying reactions in In-Li/LGPS/In-Li symmetric cell was not the ionic conduction in the LGPS electrolyte layer.

Figure 4 shows the charge-discharge cycle profiles of In-Li/LGPS/In-Li symmetric cells with HM(30 min)-LGPS and WM-LGPS collected at a current density of  $0.5 \text{ mA cm}^{-2}$ . Although the cell with HM-LGPS exhibited stable lithium alloying and dealloying for the initial 20 cycles, its overvoltage gradually increased during cell discharge. Notably, the cells with WM-LGPS did not exhibit a significant increase in overvoltage over 50 cycles. According to electrochemical investigations, the In-Li/WM-LGPS

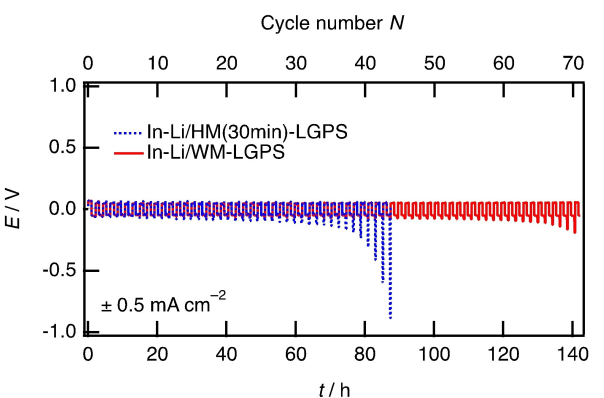


**Figure 4.** Constant-current charge and discharge profiles of In-Li/HM(30 min)-LGPS/In-Li and In-Li/WM-LGPS/In-Li symmetric cells collected at a current density of  $0.5 \text{ mA cm}^{-2}$ . The duration of each charge-discharge step was 1 h.

interface exhibited a higher reaction rate and cycle stability for lithium alloying and dealloying than the In-Li/HM-LGPS interface. Two factors determine the reaction rate and stability of alloy anode/sulfide electrolyte interfaces:<sup>[43]</sup> the formation of a resistive layer at the interface (by the reductive decomposition of the electrolyte species at low voltages) and large microstructural changes in the anode (induced by volumetric changes in metal anodes during lithium alloying and dealloying). The resistive layer is one of the main factors deteriorating the stability of Li-metal anodes with a low reaction potential. The ionically insulating layer grows during cycling, gradually decreasing the reaction rate. The second factor (large microstructural changes) leads to mechanical degradation, which restricts Li-ion diffusion pathways and causes a loss of contact between the metal anode and solid electrolyte.<sup>[44]</sup> LGPS has been reported to be sufficiently stable at the reaction potential of the In-Li anode ( $0.6 \text{ V}$  vs.  $\text{Li}/\text{Li}^+$ ).<sup>[37]</sup> Thus, the gradual growth of a resistive phase does not adequately explain the rapid increase in cell voltage observed during charge-discharge cycling. Furthermore, XRD and EIS analyses did not indicate significant differences between the bulk and surface structures of HM- and WM-LGPS, indicating similar electrochemical stability at low voltages. Thus, mechanical degradation was considered the main factor causing the increase in overvoltage in the In-Li/LGPS/In-Li symmetric cells.

#### Microstructural changes at the In-Li/LGPS interface

To understand the lithium alloying and dealloying processes at the In-Li/LGPS interface further, the microstructural changes during cycling were investigated using Field-emission scanning electron microscopy/energy-dispersive X-ray spectroscopy ((FE-)SEM/EDS). Figure 5 shows cross-sectional SEM/EDS images of the In-Li/HM-LGPS and In-Li/WM-LGPS interfaces, before and after charge-discharge at  $0.5 \text{ mA cm}^{-2}$  for 1 h per cycle. After cell fabrication, both the electrolyte layers were in sufficient contact with the In-Li anode layer. In-Li and LGPS are elastically soft (with low elastic modulus values in the range of  $3.5\text{--}4.0$ )<sup>[45]</sup>

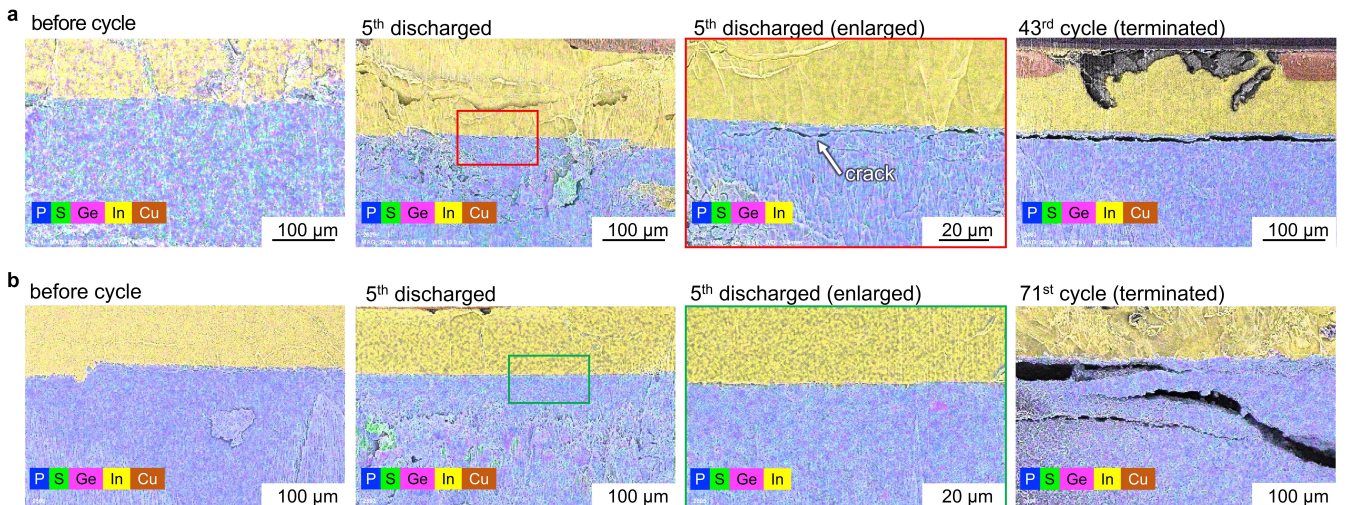


**Figure 5.** Cross-sectional SEM/EDS images of a) In-Li/HM-LGPS/In-Li and b) In-Li/WM-LGPS/In-Li symmetric cells before charge-discharge, during the 5<sup>th</sup> charge-discharge cycle, and during the terminated cycle, after an Ar-ion milling process. Each cycle involves cell charge-discharge for 1 h at 0.5 mA cm<sup>-2</sup>.

and 20.4 GPa,<sup>[46]</sup> respectively); therefore, the interfacial contact area increased (by deformation and densification) during the cell-construction pressurization process. Furthermore, EDS images indicate no interphase formation between In-Li and LGPS. Notably, interfacial contact between In-Li and HM-LGPS was retained on charging and discharging the In-Li/HM-LGPS/In-Li cell for five cycles. However, cracks were observed in the HM-LGPS layer adjacent to the In-Li/LGPS interface. Crack growth occurred parallel to the interface at the 43<sup>rd</sup> cycle, causing a large gap (~10 μm thick) that hinders lithium diffusion in the HM-LGPS electrolyte layer. This elucidates the sudden increase in overvoltage observed at the terminated cycle (shown in Figures 3 and 4). In contrast, no cracked regions were observed in the WM-LGPS layers after five cycles. Although some voids were observed in the WM-LGPS layer after the 71<sup>st</sup> cycle, some lithium-diffusion pathways were retained in the interelectrode direction. The gradual increase in overvoltage observed in the In-Li/WM-LGPS/In-Li cell could be corresponding to an increase in the diffusion distance in the WM-LGPS layer. Moreover, EDS images showed negligible changes in the chemical composition of the In-Li/HM-LGPS and In-Li/WM-LGPS interfaces, confirming no resistive-layer growth during cycling. Furthermore, no growth of In-Li dendrites was observed during the cycling. This might be due to the relatively small number of cycles and low stacking pressure compared with that of the cells reported previously.<sup>[47]</sup> Therefore, SEM/EDS indicates that the differences in the mechanical properties of the electrolyte layers determine the reversibility of the lithium alloying and dealloying reactions.

The mechanical properties of solid materials depend on the tap density of the sample and morphology of the constituent particles.<sup>[24]</sup> Poorly densified samples include a large number of voids, which can act as starting points for crack formation.<sup>[24,25]</sup> Both HM- and WM-LGPS pellets exhibited a tap density of 1.63 g cm<sup>-3</sup> under similar contact conditions with the In-Li anode before charge-discharge (Figure S6). Thus, the excellent mechanical properties of the In-Li/WM-LGPS interface can be

attributed to its particle size. According to the Hall-Petch relationship, the following equations represent semi-empirically derived relational expressions between the yield strength ( $\sigma_f$ ) and grain size ( $D$ ):<sup>[26,27]</sup>

$$\sigma_f = \sigma_0 + k_1 D^{-1/2} \quad (2)$$

$$\sigma_f = k_2 D^{-1/2} \quad (3)$$

where  $k_1$ ,  $k_2$  are constants ( $k_1 < k_2$ ), and  $\sigma_0$  indicates the friction stress, which is contributed by the particles (not dislocation). The applicability of Equations (2) or (3) depends on the grain size.<sup>[27,48–50]</sup> Equation (2) is applicable for materials with a grain size of  $< 10 \mu\text{m}$ . For grain sizes of several tens of micrometers or more, the yield strength decreases rapidly; therefore, the behavior depicted by Equation (3) is experimentally observed. Under both conditions, the fracture susceptibility of the solid sample is in proportion to the square of  $D^{-1/2}$ . For samples with large grain sizes, large dislocations accumulate at the grain boundaries, increasing the grain-boundary stress; subsequently, when the stress becomes sufficiently high to propagate to the next grain, yielding occurs. HM-LGPS, with a  $d_{50}$  of 1.32 μm, comprises particles with a size of several tens of micrometers (Figure 1). The mechanical strength of this LGPS layer is relatively low around the coarse particles, resulting in crack formation (owing to the mechanical stress induced by the large volume changes in In-Li). In contrast, WM-LGPS, with a  $d_{50}$  of 0.51 μm, exhibited a narrow size distribution with no coarse particles. The small grains with relatively high mechanical strength suppress crack formation; consequently, excellent electrochemical stability was observed during the charge-discharge cycling of In-Li with WM-LGPS. These results indicate that downsizing sulfide-electrolyte particles is crucial for improving the electrochemical reaction area and suppressing mechanical degradation during charging and discharging.

### Limiting current density of In-Li alloy electrodes

Constant current charge-discharge cycling of In-Li/LGPS/In-Li cells at different current densities and cut-off capacities was conducted to clarify the effects of the rate and degree of volume change of In-Li on the electrochemical stability of the In-Li/LGPS interface. In this study, the electrochemical stability was determined from the change in overvoltage during 10 cycles and classified into following categories: (i) stable (no change in overvoltage); (ii) operable (cycles completed with a gradual increase in overvoltage); and (iii) inoperable (severe overvoltage exceeding the voltage range of  $-10$  to  $10$  V, which indicates the device limit).

Figure 6 summarizes the regions of stable operation for the In-Li/HM-LGPS and In-Li/WM-LGPS interfaces at current densities of  $1\text{--}4\text{ mA cm}^{-2}$ . The cut-off capacities are shown as areal capacities, calculated using the contact area between the In-Li and LGPS interface. When the In-Li/HM-LGPS/In-Li cell is operated at  $1.0\text{ mA cm}^{-2}$ , the overvoltage changes negligibly during the first 10 cycles (up to a cut-off capacity of  $1.5\text{ mAh cm}^{-2}$ ). However, the overvoltage gradually increased at a cut-off capacity of  $2.0\text{ mAh cm}^{-2}$ , and the cell became inoperable at  $2.5\text{ mAh cm}^{-2}$ . This increase in overvoltage indicates a loss of physical contact owing to the delamination of the HM-LGPS layer near the interface, as shown in SEM/EDS images (Figure 5). The In-Li volume change increases with the cut-off capacity; therefore, when operated under a high cut-off capacity, the HM-LGPS layer was subjected to a large mechan-

ical stress from the In-Li electrode. Consequently, at a current density of  $2.0\text{ mA cm}^{-2}$ , the stable operation limit of the In-Li/HM-LGPS/In-Li cell was reduced to a cut-off capacity of  $1.0\text{ mAh cm}^{-2}$ . Furthermore, this cell was inoperative at high current densities ( $>2.0\text{ mA cm}^{-2}$ ). When operated under high current densities, a reaction distribution of lithium alloying and dealloying is formed at the In-Li/HM-LGPS interface; this results in a region of concentrated mechanical stress at the In-Li/HM-LGPS interface, which promotes crack formation in the HM-LGPS layer. Contrarily, the In-Li/WM-LGPS/In-Li cell showed stable lithium alloying and dealloying over 10 cycles at a current density of  $4.0\text{ mA cm}^{-2}$  and cut-off capacity of  $1.0\text{ mAh cm}^{-2}$  (Figure 6b). Therefore, using WM-LGPS (with excellent mechanical strength) suppresses crack formation under high-current-density conditions. No significant improvement was observed with respect to the large cut-off capacity under our experimental conditions.

Color-coded overpotential diagrams indicate that the In-Li/WM-LGPS interface exhibits a better electrochemical stability at higher current densities than the In-Li/HM-LGPS interface. Two-electrode cells with In-Li counter electrodes have been widely used to characterize the charge-discharge properties of cathode and anode materials in ASSBs.<sup>[37,51,52]</sup> The electrochemical instability of the In-Li/sulfide electrolyte interface adversely affects the electrochemical properties of the system, such as the current density, areal capacity of working electrodes, and cycle number. For instance, assuming a standard cathode composite of LiCoO<sub>2</sub>/HM-LGPS (5:5 volume, 10.2 mm diameter, and 12 mg weight), the areal capacity of the cell is  $\sim 1.5\text{ mAh cm}^{-2}$  (details are provided in Supporting Information S3). The current density for charging and discharging is limited to a value (less than  $1.0\text{ mA cm}^{-2}$ ) that corresponds to 0.7 C operation. Most studies on sulfide-based ASSBs report charge-discharge cycle tests below 0.5 C, possibly due to limitations of the In-Li counter electrode.<sup>[53]</sup> In contrast, the In-Li/WM-LGPS interface showed acceptable electrochemical stability at a current density of  $4.0\text{ mA cm}^{-2}$ , and could be used for rate-capability tests (of the LiCoO<sub>2</sub>/LGPS composite) above 2 C. Therefore, the In-Li/WM-LGPS interface (with high mechanical strength) facilitates an accurate evaluation of the charge-discharge characteristics of the working electrode under a wide range of measurement conditions. Additionally, improving the mechanical stability of Li and Li alloy (Li–Si, Li–Sn, Li–Mg) anodes is a vital aspect of ASSB research;<sup>[54–57]</sup> submicron-sized sulfide solid electrolytes could effectively stabilize various anode interfaces, contributing immensely to battery research.

### Conclusions

Sub-micrometer-sized LGPS solid electrolytes with a narrow size distribution were fabricated without crystallinity degradation by a wet-milling process. Although WM-LGPS shows an average particle size of  $0.51\text{ }\mu\text{m}$ , which is smaller than that of HM-LGPS ( $1.32\text{ }\mu\text{m}$ ), both WM- and HM-LGPS grains exhibit similar lithium-ion conductivity. Moreover, In-Li/LGPS/In-Li symmetric cells exhibit smaller overpotentials at the In-Li/WM-LGPS inter-

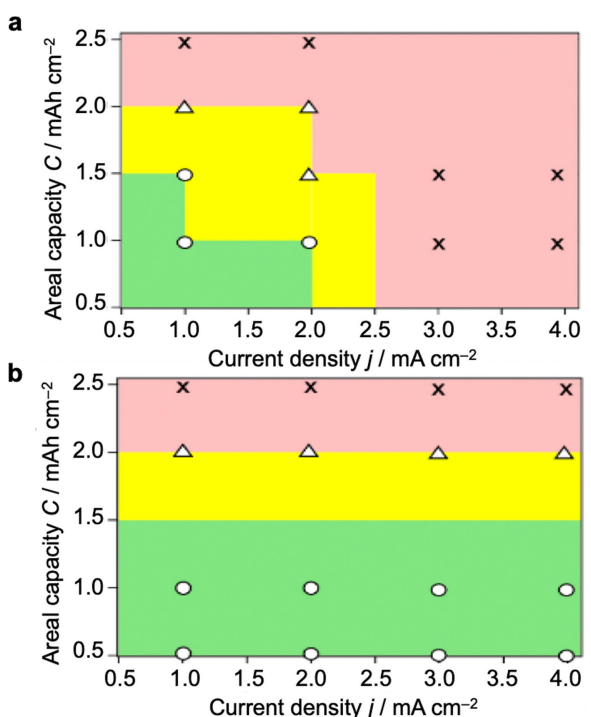


**Figure 6.** Color-coded overpotential diagrams of symmetric cells containing In-Li and a) HM- or b) WM-LGPS, after cell testing under different current densities (in the range of  $0.5\text{--}4\text{ mA cm}^{-2}$ ). Green: stable operation; yellow: exhibits overpotential growth; and red: inoperable due to high overpotentials.

face than the In-Li/HM-LGPS interface, as indicated by electrochemical charge-discharge tests. According to SEM, the higher overpotential of the latter system can be mainly attributed to the blockage of ionic conduction pathways (because of crack growth in the HM-LGPS layer adjacent to the interface). Contrarily, WM-LGPS (with submicron-sized grains) significantly suppresses crack formation, and the excellent mechanical strength of this system due to nanosizing can be explained by the Hall-Petch relationship. The improved mechanical strength of WM-LGPS can extend the operable range of In-Li alloy counter electrodes in two-electrode cells, which are widely used for evaluating the properties of ASSBs. This study confirms that downsizing sulfide-electrolyte particles is crucial for suppressing mechanical degradation at the electrode/electrolyte interface during charge-discharge cycles, thereby enhancing the stability of battery operation.

## Experimental Section

### Synthesis and pulverization of the sulfide solid electrolyte

A solid-state reaction was used to synthesize LGPS.<sup>[58]</sup> The starting materials, Li<sub>2</sub>S (Mitsuwa Chemical, 99.9%), P<sub>2</sub>S<sub>5</sub> (Aldrich, 99%), and GeS<sub>2</sub> (Kojundo Chemical Laboratory, 99.99%), were weighed in a stoichiometric ratio in an Ar-filled glove box and mixed mechanically in a ZrO<sub>2</sub> pot with ZrO<sub>2</sub> balls (10 mm in diameter) at 380 rpm for 40 h using a planetary mill (Fritsch, Pulverisette 7). The product mixture was pelletized and sealed in a quartz tube under vacuum and heated at 823 K for 8 h. After heat treatment, the LGPS pellets were pulverized in a mortar by hand milling for 5 and 30 min. Wet milling was used to fabricate smaller and more uniform LGPS particles (WM-LGPS). To fabricate WM-LGPS, hand-milled LGPS (HM-LGPS) was transferred into a ZrO<sub>2</sub> pot containing ZrO<sub>2</sub> balls (5–10 mm in diameter) and anhydrous heptane (Wako Pure Chemicals Ind., 99.0%), WM at 300 rpm for 80 min, and then dried for 12 h under vacuum.

### Structural characterization

The particle-size distributions of HM- and WM-LGPS were determined by a scanning electron microscope (JEOL, JSM-6610) and a laser scattering particle-size distribution analyzer (PSA; Horiba, Partica LA-960). An XRD instrument with Cu K $\alpha$  radiation (Rigaku, SmartLab) was used to examine the sample crystallinity.

### Electrochemical characterization

EIS was used to investigate the lithium-ion conductivity of HM- and WM-LGPS. Sample pellets with a diameter of 10.2 mm (formed under a pressure of 110 MPa) were sandwiched between Au ion-blocking electrodes, and room-temperature EIS data were collected under an applied voltage of 10 mV in the frequency range of 7 MHz to 0.1 Hz using a frequency response analyzer (Bio-Logic, VSP-300). Additionally, a frequency response analyzer (TOYO Corporation, LN-ZZ-HF) was used to record EIS data in the temperature range of 175–298 K, which were used to investigate the lithium-ion conductivity within the grains and at the grain boundaries. The temperature was regulated using a cryogenic controller (Lake Shore, Model 336).

The charge and discharge characteristics of the In-Li anode/LGPS solid electrolyte interface were investigated using In-Li/LGPS/In-Li

symmetric cells. During cell construction, LGPS (200 mg) was cold-pressed at 110 MPa in a cylindrical mold (10.2 mm in diameter), and In-Li alloy disks were sequentially placed on both sides of the LGPS layer and fixed with a torque wrench (100 MPa) without additional pressure. A potentiostat/galvanostat (Bio-Logic, VSP-300) was used for charge-discharge measurements at room temperature under current densities in the range of 0.1–4.0 mA cm<sup>-2</sup>.

### Microstructural observations at the In-Li/LGPS interface

In-Li/LGPS/In-Li symmetric cells, before and after cycling, were cut using a multi-angle slicer (JASCO, Slice Master HW-1), and the cross-sections were flattened by ion milling (Hitachi High-Tech, IM4000 plus).<sup>[59]</sup> Field-emission (FE) SEM (Hitachi High-Tech; Regulus 8230) and energy-dispersive X-ray spectroscopy (EDS) (Bruker, QUANTAX FlatQUAD) were used to investigate the cross-sectional images of In-Li/LGPS/In-Li symmetric cells. FE-SEM and EDS were conducted under an acceleration voltage of 10 keV and emission current of 10  $\mu$ A.

### Acknowledgements

This study was partially supported by a Grant-in-Aid for Scientific Research in Innovative Areas (No. 19H05793) from the Japan Society for the Promotion of Science.

### Conflict of Interests

The authors declare no conflict of interest.

### Data Availability Statement

Research data are not shared.

**Keywords:** all-solid-state batteries • solid electrolyte • grain boundary strengthening • mechanical properties • LGPS

- [1] N. Kamaya, K. Homma, Y. Yamakawa, M. Hirayama, R. Kanno, M. Yonemura, T. Kamiyama, Y. Kato, S. Hama, K. Kawamoto, A. Mitsui, *Nat. Mater.* **2011**, *10*, 682.
- [2] K. Takada, *J. Power Sources* **2018**, *394*, 74.
- [3] J. Janek, W. G. Zeier, *Nat. Energy* **2016**, *1*, 16141.
- [4] Y. Kato, S. Shiotani, K. Morita, K. Suzuki, M. Hirayama, R. Kanno, *J. Phys. Chem. Lett.* **2018**, *9*, 607.
- [5] R. Koerver, I. Aygun, T. Leichtweib, C. Dietrich, W. Zhang, J. O. Binder, P. Hartmann, W. G. Zeier, J. Janek, *Chem. Mater.* **2017**, *29*, 5574.
- [6] D. Y. Oh, Y. J. Nam, K. H. Park, S. H. Jung, S.-J. Cho, Y. K. Kim, Y.-G. Lee, S.-Y. Lee, Y. S. Jung, *Adv. Energy Mater.* **2015**, *5*, 1500865.
- [7] A. Sakuda, A. Hayashi, M. Tatsumisago, *Sci. Rep.* **2013**, *3*, 2261.
- [8] A. Hayashi, A. Sakuda, M. Tatsumisago, *Front. Energy Res.* **2016**, *4*, 25.
- [9] Q. Tu, L. Barroso-Luque, T. Shi, G. Cedar, *Cell Rep. Phys. Sci.* **2020**, *1*, 100106.
- [10] J.-M. Doux, H. Nguyen, D. H. S. Tan, A. Banerjee, X. Wang, E. A. Wu, C. Jo, H. Yang, Y. S. Meng, *Adv. Energy Mater.* **2020**, *10*, 1903253.
- [11] Y. Han, S. H. Jung, H. Kwak, S. Jun, H. H. Kwak, J. H. Lee, S.-T. Hong, Y. S. Jung, *Adv. Energy Mater.* **2021**, *11*, 2100126.
- [12] R. Chen, Q. Li, X. Yu, L. Chen, H. Li, *Chem. Rev.* **2020**, *120*, 6820.
- [13] M. Otoyama, H. Kowada, A. Sakuda, M. Tatsumisago, A. Hayashi, *J. Phys. Chem. Lett.* **2020**, *11*, 900.
- [14] J. O. Besenhard, J. Yang, M. Winter, *J. Power Sources* **1997**, *68*, 87.

- [15] H. Li, T. Yamaguchi, S. Matsumoto, H. Hoshikawa, T. Kumagai, N. L. Okamoto, T. Ichitsubo, *Nat. Commun.* **2020**, *11*, 1584.
- [16] A. Kato, A. Hayashi, M. Tatsumisago, *J. Power Sources* **2016**, *309*, 27.
- [17] A. Parejiya, R. Amin, M. B. Dixit, R. Essehli, C. J. Jafta, D. L. Wood III, I. Belharouak, *ACS Energy Lett.* **2021**, *6*, 3669.
- [18] Y. Su, L. Ye, W. Fitzhugh, Y. Wang, E. Gil-Gonzalez, I. Kim, X. Li, *Energy Environ. Sci.* **2020**, *13*, 908.
- [19] K. K. Eckhardt, P. J. Klar, J. Janek, C. Heiliger, *ACS Appl. Mater. Interfaces* **2022**, *14*, 35545.
- [20] Y.-H. Wang, J. Yue, W.-P. Wang, W.-P. Chen, Y. Zhang, Y.-G. Yang, J. Zhang, Y.-X. Yin, X. Zhang, S. Xin, Y.-G. Guo, *Mater. Chem. Front.* **2021**, *5*, 5328.
- [21] S. Noh, W. T. Nichols, C. Park, D. Shin, *Ceram. Int.* **2017**, *43*, 15952.
- [22] A. Bielefeld, D. A. Weber, J. Janek, *J. Phys. Chem. C* **2018**, *123*, 1626.
- [23] Y. Yamada, K. Watanabe, H. S. Kim, K. Suzuki, S. Hori, R. Kanno, M. Hirayama, *Batteries & Supercaps* **2023**, e202300261.
- [24] K. R. Kambale, A. Mahajan, S. P. Butee, *Met. Powder Rep.* **2019**, *74*, 130.
- [25] W. Yuan, S. K. Panigrahi, J. Q. Su, R. S. Mishra, *Scr. Mater.* **2011**, *65*(11), 994–997.
- [26] N. Hansen, *Scr. Mater.* **2004**, *51*, 801.
- [27] S. C. Carniglia, *J. Am. Ceram. Soc.* **1965**, *48*, 580.
- [28] D. Tian, C.-J. Zhou, J.-H. HE, *Text. Res. J.* **2019**, *89*, 1340.
- [29] J. J. Roa, E. Jimenez-Pique, J. M. Tarrago, D. A. Sandoval, A. Mateo, J. Fair, L. Llanes, *Mat. Sci. Eng. A* **2016**, *676*, 487.
- [30] B. Kang, J. Lee, H. J. Ryu, S. Y. Hong, *J. Alloys Compd.* **2018**, *767*, 1012.
- [31] R. Ren, J. Fan, B. Wang, Q. Zhang, W. Li, H. Dong, *J. Alloys Compd.* **2022**, *920*, 165924.
- [32] N. Abid, A. M. Khan, S. Shujait, K. Chaudhary, M. Ikram, M. Imran, J. Haider, M. Khan, Q. Khan, M. Maqbool, *Adv. Colloid Interface Sci.* **2022**, *300*, 102597.
- [33] K. Yamamoto, M. Takahashi, K. Ohara, N. H. H. Phuc, S. Yang, T. Watanabe, T. Uchiyama, A. Sakuda, A. Hayashi, M. Tatsumisago, H. Muto, A. Matsuda, Y. Uchimoto, *ACS Omega* **2020**, *5*, 26287.
- [34] A. Miura, N. C. Rosero-Navarro, A. Sakuda, K. Tadanaga, N. H. H. Phuc, A. Matsuda, N. Machida, A. Hayashi, M. Tatsumisago, *Nat. Rev. Chem.* **2019**, *3*, 189.
- [35] T. Shi, Q. Tu, Y. Tian, Y. Xiao, L. J. Miara, O. Kononova, G. Cedar, *Adv. Energy Mater.* **2020**, *10*, 1902881.
- [36] G. Oh, M. Hirayama, O. Kwon, K. Suzuki, R. Kanno, *Chem. Mater.* **2016**, *28*, 2634.
- [37] A. L. Santhosha, L. Medenbach, D. J. R. Buchheim, P. D. P. Adelhelm, *Batteries & Supercaps* **2019**, *2*, 524.
- [38] Y. Sun, K. Suzuki, S. Hori, M. Hirayama, R. Kanno, *Chem. Mater.* **2017**, *29*, 5858.
- [39] P. Bron, S. Dehnens, B. Roling, *J. Power Sources* **2016**, *329*, 530.
- [40] Y. Jin, Q. He, G. Liu, Z. Gu, M. Wu, T. Sun, Z. Zhang, L. Huang, X. Yao, *Adv. Mater.* **2023**, *35*, 2211047.
- [41] J. Wu, S. Liu, F. Han, X. Yao, C. Wang, *Adv. Mater.* **2021**, *33*(6), 2000751.
- [42] X. Zhao, P. Xiang, J. Wu, Z. Liu, L. Shen, G. Liu, Z. Tian, L. Chen, X. Yao, *Nano Lett.* **2022**, *23*(1), 227–234.
- [43] A. Banerjee, X. Wang, C. Fang, E. A. Wu, Y. S. Meng, *Chem. Rev.* **2020**, *120*, 6878.
- [44] E. Kazyak, R. Garcia-Mendez, W. S. LePage, A. Sharifi, A. L. Davis, A. J. Sanchez, K.-H. Chen, C. Haslam, J. Sakamoto, N. P. Dasgupta, *Matter* **2020**, *2*, 1025.
- [45] E. A. Il'ina, K. V. Druzhinin, E. D. Lyalin, M. S. Plekhanov, I. I. Talankin, B. D. Antonov, A. A. Pnukratov, *J. Mater. Sci.* **2022**, *57*, 1291.
- [46] Z. Q. Wang, M. S. Wu, G. Liu, X. L. Lei, B. Xu, C. Y. Ouyang, *Int. J. Electrochem. Sci.* **2014**, *9*(2), 562.
- [47] S. Luo, Z. Wang, X. Li, X. Liu, H. Wang, W. Ma, L. Zhang, L. Zhu, X. Zhang, *Nat. Commun.* **2021**, *12*(1), 6968.
- [48] T. Vasilos, J. B. Mitchell, R. M. Spriggs, *J. Am. Ceram. Soc.* **1964**, *47*, 606.
- [49] R. M. Spriggs, J. B. Mitchell, T. Vasilos, *J. Am. Ceram. Soc.* **1964**, *47*, 323.
- [50] R. E. Fryxell, B. A. Chandler, *J. Am. Ceram. Soc.* **1964**, *47*, 283.
- [51] X. Wu, M. El Kazzi, C. Villevieille, *J. Electroceram.* **2017**, *38*, 207.
- [52] P. Bonnick, K. Niitani, M. Nose, K. Suto, T. S. Arthur, J. Muldoon, *J. Mater. Chem. A* **2019**, *7*, 24173.
- [53] X. Bai, T. Yu, Z. Ren, S. Gong, R. Yang, C. Zhao, *Energy Storage Mater.* **2022**, *51*, 527.
- [54] Y. Huang, B. Shao, F. Han, *J. Mater. Chem. A* **2022**, *10*, 12350.
- [55] S. Y. Han, C. Lee, J. A. Lewis, D. Yeh, Y. Liu, H.-W. Lee, M. T. McDowell, *Joule* **2021**, *5*, 2450.
- [56] M. Kim, M. J. Kim, Y. S. Oh, S. Kang, T. H. Shin, H.-T. Lim, *Adv. Sci.* **2023**, *2301381*.
- [57] M. Siniscalchi, J. Liu, J. S. Gibson, S. J. Turrell, J. Aspinall, R. S. Weatherup, M. Pasta, S. C. Speller, C. R. M. Grovenor, *ACS Energy Lett.* **2022**, *7*, 3593.
- [58] O. Kwon, M. Hirayama, K. Suzuki, Y. Kato, T. Saito, M. Yonemura, T. Kamiyama, R. Kanno, *J. Mater. Chem. A* **2015**, *3*, 438.
- [59] T. Yabuzaki, M. Sato, H. Kim, K. Watanabe, N. Matui, K. Suzuki, Hori, K. Hikima, S. Obokata, H. Muto, A. Matsuda, R. Kanno, M. Hirayama, *J. Ceram. Soc. Jpn.* **2023**, doi: 10.2109/jcersj2.23070.

Manuscript received: July 11, 2023

Revised manuscript received: August 15, 2023

Accepted manuscript online: August 18, 2023

Version of record online: August 28, 2023